

# In-situ observation of microstructural evolution in reheated low carbon bainite weld metals with various Ni contents

Gao-jun Mao<sup>1,2</sup>, Rui Cao<sup>1,2,\*</sup>, Jian-hong Chen<sup>1,2,\*</sup>, Xi-li Guo<sup>3</sup>, Yong Jiang<sup>3</sup>

<sup>1</sup> Department of Materials Science and Engineering, Lanzhou University of Technology, Lanzhou 730050, Gansu, China

<sup>2</sup> State Key Laboratory of Advanced Processing and Recycling of Non-ferrous Metals, Lanzhou University of Technology, Lanzhou 730050, Gansu, China

<sup>3</sup> Atlantic China Welding Consumables, Inc., Zigong 643000, Sichuan, China

## ARTICLE INFO

**Key words:**  
Weld metal  
Ni content  
Bainite  
Nucleation site  
Growth  
In-situ observation

## ABSTRACT

Microstructural evolution in weld metals was in-situ observed through utilizing a laser scanning confocal microscope at two cooling rates. The specimens with various nickel contents were adopted for the observation. In the specimen with low fraction of Ni ( $\leq 2$  wt. %), granular bainite microstructure (i. e. broad surface relief) transformation from intragranular nucleation site was in-situ observed, while, lath bainite microstructure originating from grain boundary of austenite was in-situ observed for specimens with high mass percentage of Ni ( $\geq 4$  wt. %). With increasing nickel content, the transformation temperature dropped. The prior austenite grain size was initially depressed and subsequently coarsened dramatically with the addition of Ni. The microstructure difference was ascribed to various nucleation sites and growth direction in the matrix. On account of those observations, not only the chemical component, cooling rate and microstructure were systematically correlated, but also the microstructural evolution was definite.

## 1. Introduction

Bainite has exhibited its great importance in steel technology nowadays for the sake of obtaining the best balance between ductility and strength<sup>[1,2]</sup>. In order to increase ductility in weld metal (WM), the stimulated formation of bainitic microstructure is one of the alternatives that are being conceived nowadays to produce a finer microstructure<sup>[3]</sup>. It is reported that, for the bainitic microstructures, the cleavage fracture resistance is greatly affected by not only prior austenite size but also bainite packet size<sup>[4]</sup>. Among the alloying elements of low carbon martensitic/bainitic steels, an increase in nickel content was found to be an effective way to improve both the strength and the fracture toughness<sup>[5]</sup>. Small columnar crystals were closely linked with a lower  $Ni_{eq}$  (Ni equivalent) causing a peritectic reaction as the weld metal solidified, whilst very large columnar crystals were generated owing to a higher  $Ni_{eq}$  since the liquid metal in the weld pool could directly solidify into austenite and continuously grow afterwards<sup>[6]</sup>. In addition, the existence of Ni can

raise  $T_0$ <sup>[7]</sup>, one temperature when identical carbon content exists for both ferrite and austenite under the condition of quasi-equilibrium, which is conducive to the formation of the thin retained austenite and carbonless lath bainite and the reduction of large M-A islands<sup>[8]</sup>. So far, several researches on bainite transformation have been reported<sup>[9–12]</sup>; however, traditional metallographic investigation was employed in most previous publications. Regarding the microstructural development of low carbon weld metal, various cooling rates were investigated in the transformation process of the WMs by Komiozo<sup>[13]</sup>. On one hand, a high temperature laser scanning confocal microscope (LSCM) was used to analyze the morphological change in the cooling process, which made it probable to observe the phase transformation in real time<sup>[14]</sup>. However, the bainite morphology after transformation could only be detected through conventional metallographic investigation once, and the continuous nucleation and growth process of bainite cannot be achieved. Real-time observation of bainite transformation could be carried out incessantly, since utilizing LSCM shows

\* Corresponding author. Prof.

E-mail address: caorui@lut.cn (R. Cao); zchen@lut.cn (J.H. Chen).

more advantages over conventional methods. Only a few publications on bainite transformation were related with in-situ observation methodology<sup>[15–18]</sup>. Kang et al.<sup>[15]</sup> researched bainite nucleation and growth via in-situ transmission electron microscope observation. Zhang et al.<sup>[16]</sup> investigated bainite transformation in a 0.15% C steel by means of LSCM. Hidenori et al.<sup>[17]</sup> studied the visualization and analysis of variant grouping in continuously cooled low-carbon steel welds by LSCM. Additionally, Kolmskog et al.<sup>[18]</sup> elucidated the phenomenon of bainite formation when the experiment temperature was below martensite start temperature ( $M_s$ ) by LSCM. On the other hand, the microstructures in weld heat affected zones (HAZ) were found to increase probability of cleavage fracture<sup>[19]</sup>; thus, it is of necessity to research microstructure features in weld reheated zones. Microstructural formation of reheated zones in WM can be successfully simulated by LSCM experimental procedures.

However, little attention has been paid to the effect of Ni on the microstructural evolution and morphological development of reheated zones in WM directly. In this paper, via in-situ observations with the aid of LSCM, both the chemical composition and cooling rate are correlated with microstructure systematically.

## 2. Experimental Procedures

The Q345 high strength low alloy steels were automatically gas metal arc welded using a single consumable with diverse degrees of Ni in the metal power flux-cored wires to design WMs with various chemical compositions. Before welding, base metal plates were cleaned. Buttering welding was performed in 20 mm deep V-groove in the Q345 steel plate to avoid the dilution of the WM by the base metal, before the deposition of the first-pass weld bead. Under the identical welding conditions, four groups of specimens (W1, W2, W3 and W4) were made in the laboratory with diverse degrees of Ni in WM. The chemical composition of Q345 steel and the planned Ni contents added in metal powder weld wires are given in Tables 1 and 2, respectively. The physical welding processes are listed in Table 3. The electrical data of the welding process are listed in Table 4. All of the mentioned assignments were carried out in the Atlantic China Welding Consumables, Inc., Zigong. The chemical compositions of the

**Table 1**

Chemical composition of Q345 steel (wt.%)

C	Mn	Si	S	P	Nb	V	Ti
0.2	1.6	0.55	0.025	0.025	0.015	0.15	0.1

**Table 2**

Designed content of Ni for four kinds of metal powder cored wires (wt.%)

Weld sample	Ni added in WM
W1	Ni0
W2	Ni2
W3	Ni4
W4	Ni5

**Table 3**

Physical parameters for welding processes

Plate type	Flat
Plate size/mm×mm×mm	450×250×28
Wire grade	CHT120CK4
Wire type	GB/T17493E83C-K4
Wire diameter/mm	1.6
Cooling after welding	Air
Backing material	Q345 steel bar
Root/mm	12
Included angle/(°)	60
Shielded gas	95% Ar+5% CO <sub>2</sub>
Interpass temperature/°C	100
Electrode stickout/mm	25
Electrode separation/mm	15
Electrode diameter/mm	1.6
Direct current/A	4.76
Alternating current/A	3.97
Electrode angle to direction of welding/(°)	60

WM are presented in Table 5. In general, the Ni contents were sustained expectedly normal.

The schematic diagram of the V-type joint by multi-pass welding is shown in Fig. 1, and the former pass is the back sealing welding. Specimens for LSCM were machined to a cylinder of 6 mm×2 mm (diameter×height), also shown in Fig. 1. To maintain a level surface, both top and bottom surfaces of the specimens were polished mechanically<sup>[20]</sup>. The investigations were carried out through a VL2000DX SVF17SP LSCM, as schematically depicted in Fig. 2. Using a confocal optical system, the scanning speed of the photoacoustic element was 30 frames per sec-

**Table 4**

Electrical parameters of welding processes

Voltage/ V	Current/ A	Deposition rate, $v/(kg \cdot h^{-1})$	Electrode feed rate/ $(mm \cdot s^{-1})$	Welding speed/ $(mm \cdot s^{-1})$	Heat input, $E/(kJ \cdot mm^{-1})$
29	240	22–68	25.2	26.2	2.0 ( $\eta=0.9$ )

Note:  $\eta$ —Welding efficiency.

**Table 5**  
Chemical compositions of weld metals (wt.%)

Weld sample		C	Mn+Si	S	P	Cr+Mo	Ni	V+Cu
W1	Ni0	0.045	1.89	0.0070	0.010	1.56	0.01	0.020
W2	Ni2	0.053	1.86	0.0089	0.014	1.57	1.96	0.020
W3	Ni4	0.052	1.88	0.0095	0.013	1.55	3.65	0.020
W4	Ni5	0.043	1.85	0.0058	0.007	1.54	4.94	0.021

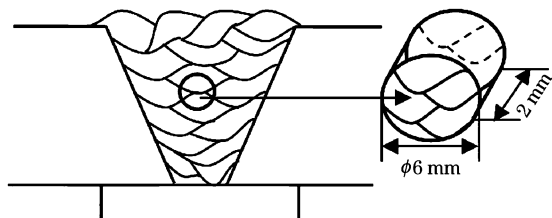


**Fig. 1.** Schematic of welding pass sequence and specimen.

austenitizing temperature of 1350 °C at 5 °C/s and held isothermally for 4 min. Subsequently, the specimens were cooled to room temperature at 5 °C/s. Moreover, another test proceeded with the same procedure before cooling process, except that the specimens were immediately cooled to 800 °C at 5 °C/s, followed by cooling at 1 °C/s to 300 °C where bainite transformation finished, and finally cooled to room temperature at 5 °C/s.

### 3. Results and Discussion

#### 3.1. In-situ observation of phase transformation

The principle for in-situ observation of bainite nucleation and growth is the relief phenomenon occurring in phase transformation, which was first observed by Ko and Cottrell in 1952<sup>[22]</sup>. Two typical morphological evolutions of bainite transformation were selected to represent all processes: less-lath shaped and lath morphological evolution.

(1)  $w(\text{Ni}) \leq 2\%$ : specimen W2 cooled at 5 °C/s was regarded as an example for less-lath-shaped morphological evolution. For the specimen cooled below bainite transformation start temperature, bainite transformation occurs along the austenite grain boundaries where the crystal nuclei form, as shown at site 1 in Fig. 4(a). New phase grows continuously into the grain (Fig. 4(b), site 2) with reducing temperature. When the temperature reaches a certain value (501.2 °C for specimen W2), the quantity of bainite transformation is about 50%, always initiating from the grain boundary transformation, as is depicted in Fig. 4(c). Finally, the phase transformation ends (Fig. 4(d)), and  $\gamma \rightarrow \alpha$  phase transformation always starts from the grain boundary and terminates in the grain across the duration of the test. It is easy for grain boundary with higher energy to satisfy energy fluctuation condition for phase transformation. Additionally, considerable dislocations, lots of vacancies and other defects exist simultaneously along the grain boundary, and thus the diffusion velocity of the solute atoms is much faster<sup>[16]</sup>. As a result, new phase is primarily nucleated at grain boundaries and grows to the interior of grain.

(2)  $w(\text{Ni}) \geq 4\%$ : specimen W4 cooled at 5 °C/s was selected for lath morphological evolution. As is depicted in Fig. 5(a), the bainitic ferrite takes place first

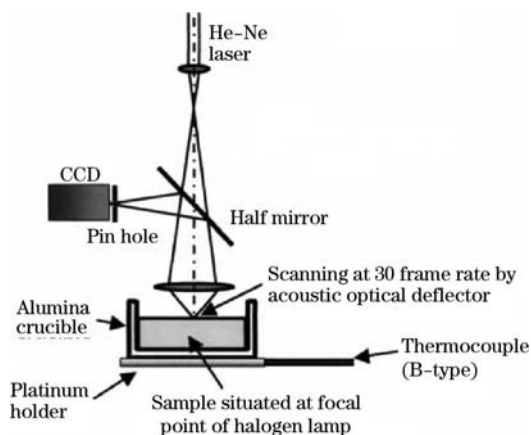


**Fig. 2.** Schematic illustration for an optical system in high temperature laser scanning confocal microscope.

ond, and only the focal point was detected by the charge coupled device (CCD) camera that can remove the effects of high temperature radiation<sup>[21]</sup>. Test procedures are shown in Fig. 3. The specimens were heated to 200 °C at 0.8 °C/s, and then heated to

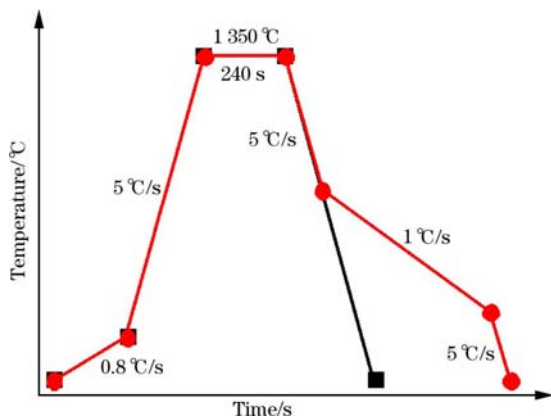
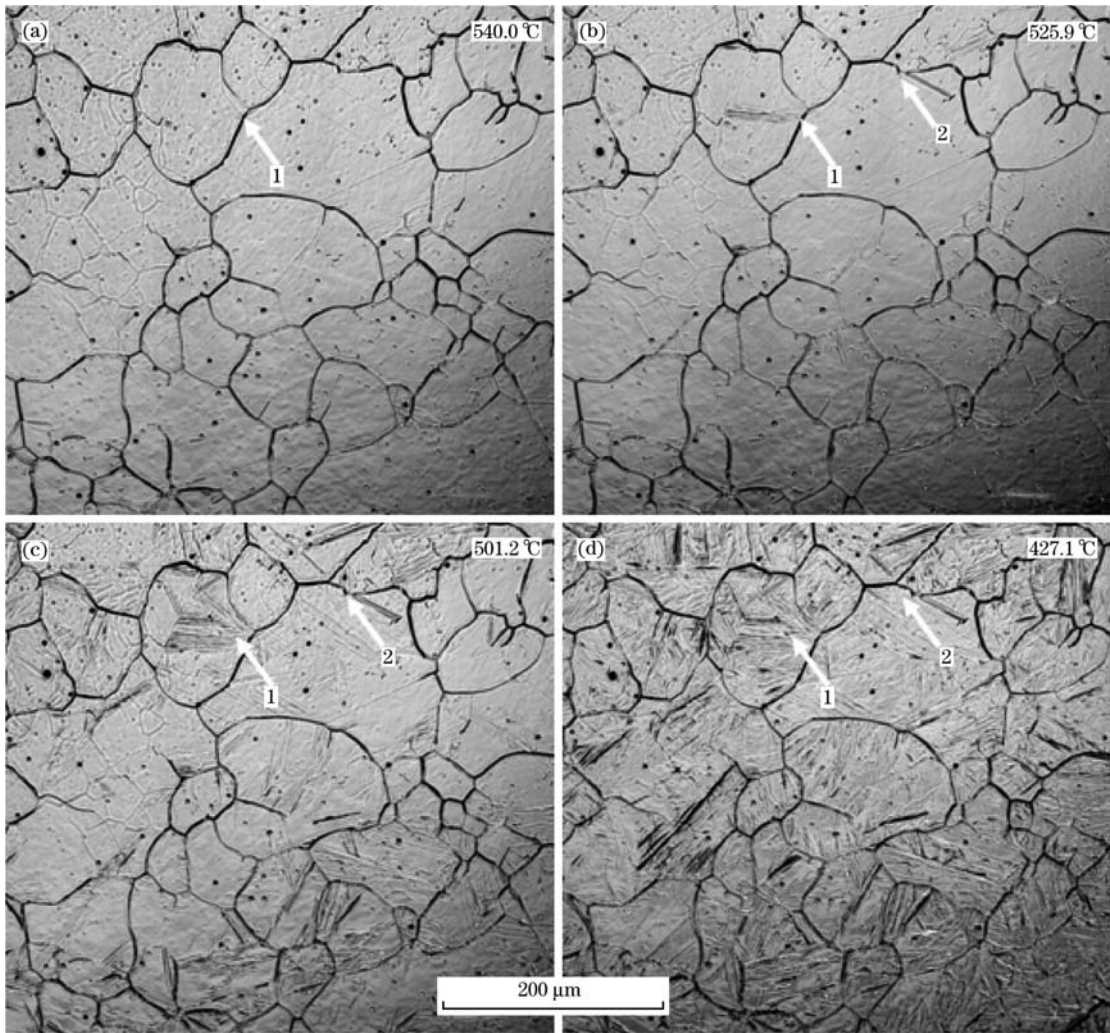


**Fig. 3.** Test procedures for in-situ observations of bainite weld metal.



(a) Start of phase transformation; (b) Continuous growth of new phase;  
(c) About 50% phase transformation; (d) Completion of phase transformation.

**Fig. 4.** In-situ observation of  $\gamma \rightarrow \alpha$  phase transformation by LSCM at 5 °C/s of specimen W2.

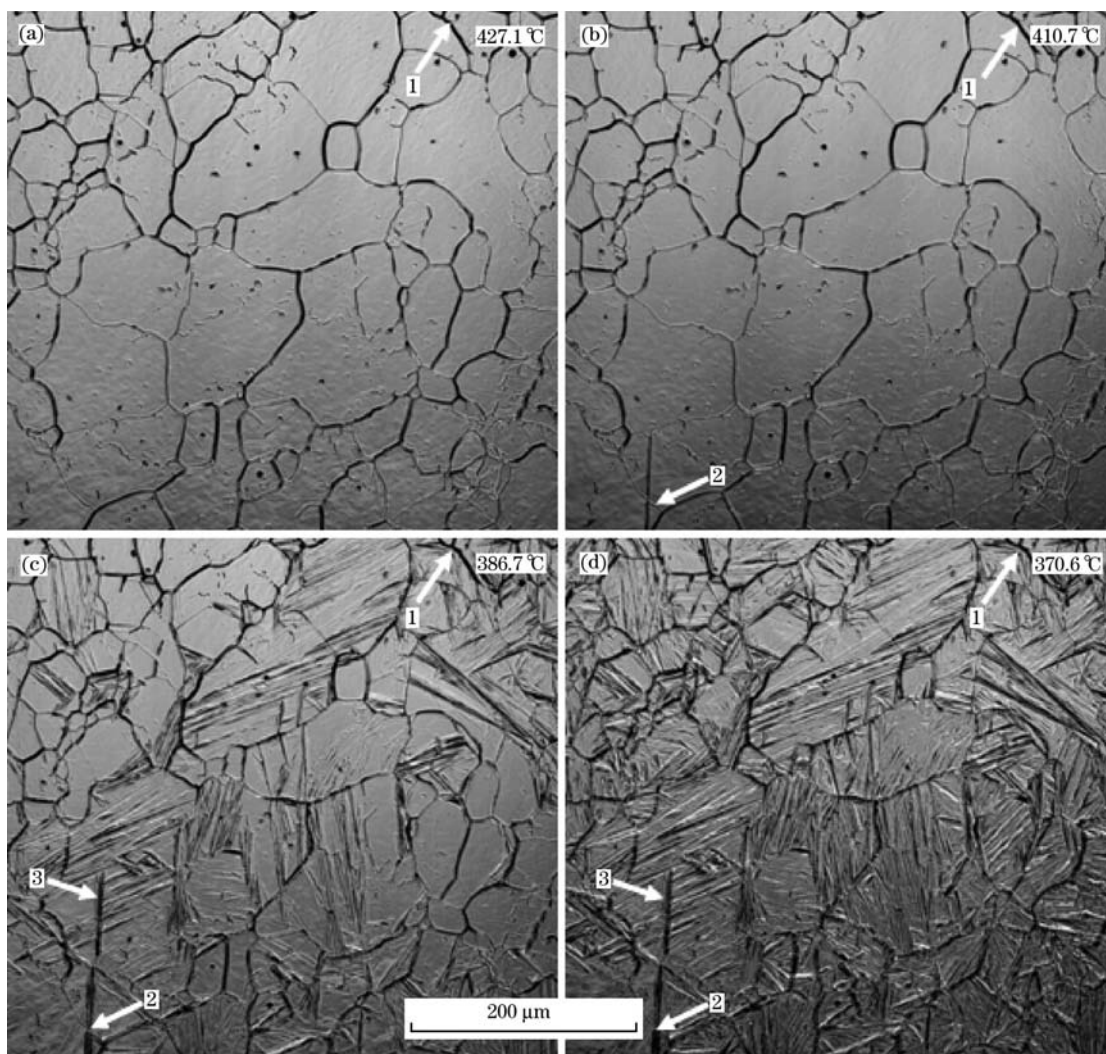
at site 1, where an inclusion precipitated inside the grain. Site 2 in Fig. 5(b) shows bainite that nucleates on the boundary. Moreover, the secondary bainitic ferrites are concurrently nucleated on the broad side/surface of the primary bainitic ferrite, and grow side-by-side in Fig. 5(c) (site 3). By the sympathetic nucleation, the bainitic ferrites increase rapidly, finally causing impingement between the bainitic ferrites. This interlocking phenomenon and the bainitic ferrite impingement are shown in Fig. 6 (c, d, g, h). As previously described, the bainitic ferrites are not only parallel to each other causing impingement, but develop in one direction same to primary bainitic ferrite.

### 3.2. Final surface morphology

Fig. 6 shows the final morphology of various specimens at different cooling rates. When  $w(\text{Ni}) \approx 0$ , flat state can be observed after transformation re-

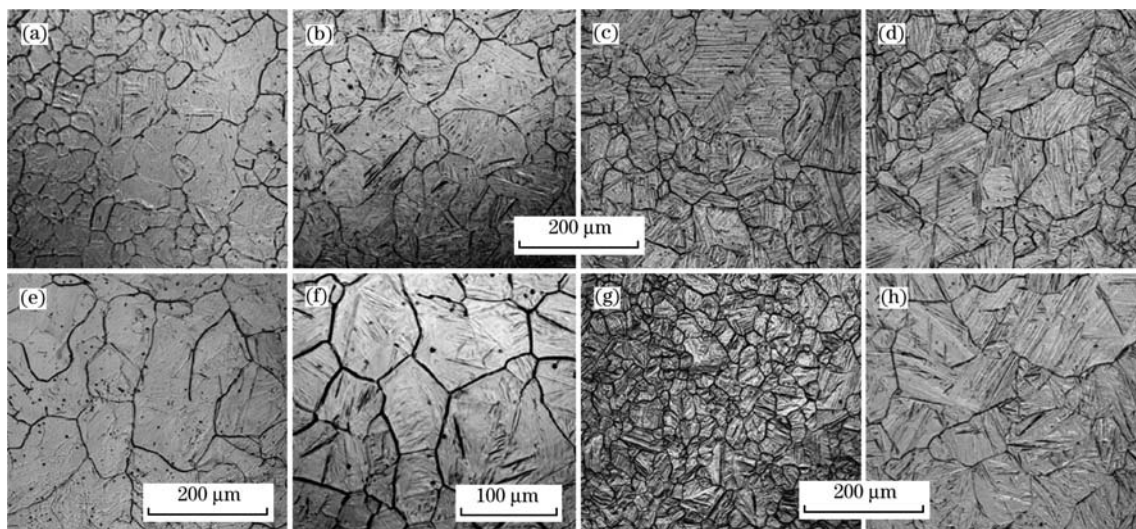
gardless of cooling rate of the specimen, as shown in Fig. 6(a,e). In addition, a minority of inconspicuous surface relief can be found with 2% Ni content, from the real-time recorded video, and it is of great interest to find that most of relief phenomenon starts at the boundary, where boundary energy provides more opportunity to nucleate than that inside the grain. Finally, when the Ni content is above 4%, bainite lath morphology appears. Nucleation sites of bainite can be categorized into two types: one is grain boundary and inclusions along which primary bainitic ferrite is nucleated, and the other is broad side/surface of the primary bainitic ferrite on which sympathetic nucleation takes place<sup>[23]</sup>.

Overall, it is easy to notice that the surface relief degree of specimens at the cooling rate of 5 °C/s presents more seriously than that of specimens cooled at 1 °C/s. On one hand, higher driving force value was obtained for phase transformation owing to



(a) Start of phase transformation; (b) Various nucleation sites of new phase;  
(c) About 50% phase transformation; (d) Completion of phase transformation.

**Fig. 5.** In-situ observation of  $\gamma \rightarrow \alpha$  phase transformation by LSCM at 5 °C/s of specimen W4.



(a) W1, 5 °C/s; (b) W2, 5 °C/s; (c) W3, 5 °C/s; (d) W4, 5 °C/s; (e) W1, 1 °C/s;  
(f) W2, 1 °C/s; (g) W3, 1 °C/s; (h) W4, 1 °C/s.

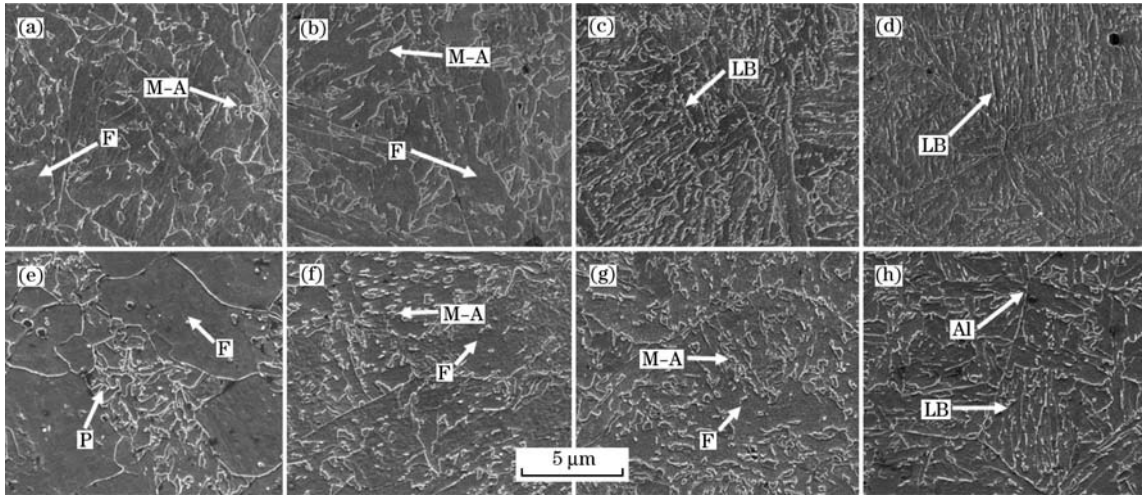
**Fig. 6.** In-situ observation of final morphology on surface of specimens when cooling at different rates.

extending degree of supercooling caused by faster cooling. In addition, as the cooling rate extends, the supercooling degree increases but the atomic diffusion velocity decreases, which reduces the start temperature and start time of the phase transformation, as is shown in Fig. 6. On the other hand, preferred nucleation sites for precipitated carbides can be attributed to the undissolved alloying element enriched precipitates<sup>[24,25]</sup>. Furthermore, alloying elements

carbonitrides are much easier to precipitate along the grain boundary at a lower cooling rate, and the carbonitrides precipitate in the grain with the increase of cooling rate<sup>[26]</sup>, which makes a huge amount of surface relief occur.

### 3.3. Analysis of microstructure

Fig. 7 shows the microstructures of the four specimens W1–W4, with varying Ni contents, after they



(a) W1, 5 °C/s; (b) W2, 5 °C/s; (c) W3, 5 °C/s; (d) W4, 5 °C/s; (e) W1, 1 °C/s;  
(f) W2, 1 °C/s; (g) W3, 1 °C/s; (h) W4, 1 °C/s.

**Fig. 7.** Final microstructure of specimens cooled at different rates.

experienced various heat cycles.

Various kinds of microstructures are mainly determined by composition and cooling rate. As the cooling rate increases, the microstructures become well refined (Fig. 7). The higher cooling rate decreases bainite transformation start temperature, at the beginning of which a few nucleation sites can be found and product phase grows rather slowly<sup>[27]</sup>. However, the supercooling degree increases owing to this higher cooling rate. Subsequently, both the driving force of phase transformation and the nucleation rate increase. Therefore, the microstructures after phase transformation are refined constantly. At the cooling rate of 1 °C/s, ferrite next to the grain boundary can be observed, and the ferrite width becomes larger (Figs. 6 (e) and 7 (e)) with the decrease of cooling rate. And the width rises from about 2.5 μm at 5 °C/s to 10 μm at 1 °C/s.

At 5 °C/s, bainite microstructure is observed, which is a mixture of ferrite matrix and martensite-austenite constituent (Fig. 7(c,d)). Proeutectoid reaction and the eutectoid transformation were suppressed owing to a higher cooling rate. Displacive transformation produces bainite<sup>[28]</sup>. Bainitic ferrite nucleus form easily on the austenite grain boundaries, and then bainitic ferrites develop in a row along the habit plane in the grain. During development,

carbon atoms redistribution emerges though atoms of alloying elements were incapable of being redistributed<sup>[29]</sup>. Between the bainitic ferrites, carbides form with the growth of the ferrite bars. Specifically, high content of Ni makes the microstructure change from granular bainite, to mixed bainitic ferrite plus granular bainite, and to a mixed lath bainitic ferrite further with the increase in cooling rate. In Fig. 7(c,d), the polygonal ferrite cannot be formed even at the lower cooling rate at the higher content of Ni ( $\geq 4$  wt. %), which may mainly include an increasing content of Ni, the conjunct addition of other alloying elements (such as Nb, Cr and Mn, etc.) into the WM, and the synergistic effect among these alloying elements contributing to bainite transformation<sup>[30]</sup>. In addition, the kinetics of transformation as well as the morphology of microstructure have been influenced by austenite grain size. For instance, the transformation temperature can be improved for larger austenite grains compared with smaller ones<sup>[31]</sup>. Moreover, long and wide bainitic sheaves formed since enough space can be offered by larger austenite grains (Fig. 6(d,h)), and this acts as an essential factor to make the final grain size of microstructures coarsen.

In conclusion, at lower levels of Ni ( $\leq 2$  wt. %), the type of microstructure hardly depends on the Ni

content but at which cooling rate the specimens were employed; on the contrary, when Ni content arrives at a high level ( $\geq 4$  wt. %), lath bainite dominates the majority of microstructure at any cooling rate.

### 3.4. Transformation temperature

As is illustrated in Ref. [32], the start and end temperatures of the phase transformation can be measured under various cooling rates in the LSCM experiments. As aforementioned, the higher cooling rate helps to decrease the start temperature of phase transformation but makes supercooling degree enlarged, which means that the gap value  $B_s - B_f$  between start temperature  $B_s$  and finishing temperature  $B_f$  of bainite transformation at 5 °C/s is lower than that at 1 °C/s (Fig. 8). During phase transformation, the driving force rises, the critical nucleation energy falls, and the nucleation rate increases, all of which lead to urgent completion of bainite transformation. From a different perspective, with the increment of Ni content, the value of  $B_s$ ,  $B_f$  and  $B_s - B_f$  decreases respectively.

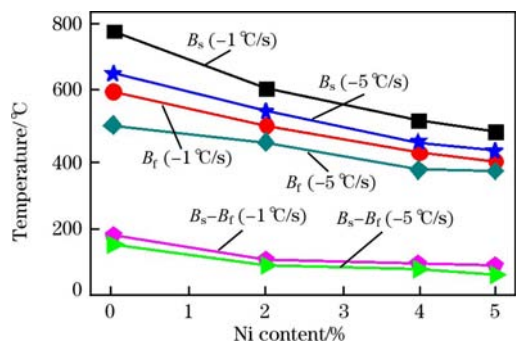
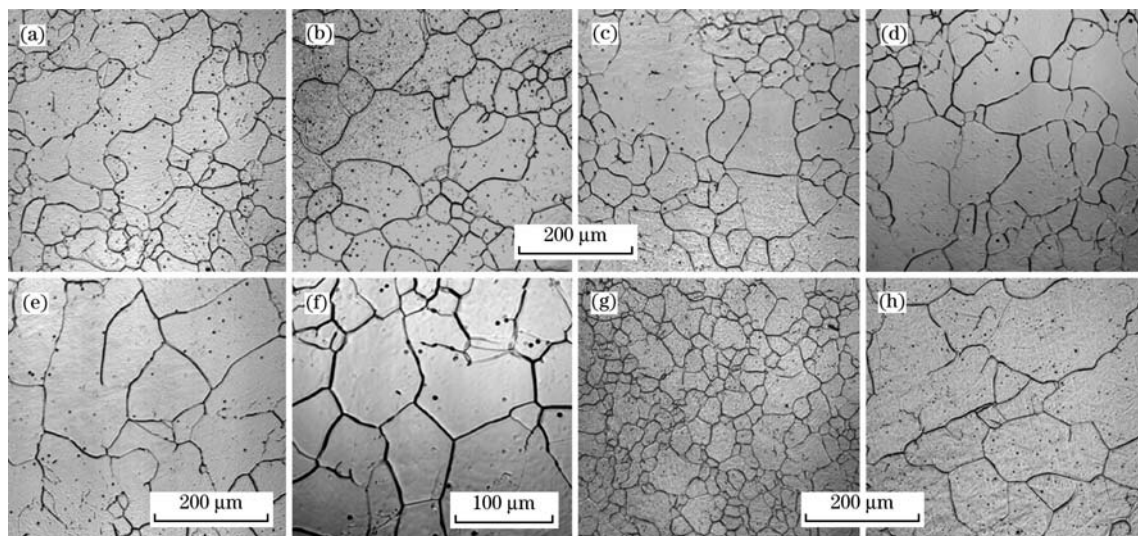


**Fig. 8.** Variation of  $B_s$ ,  $B_f$  and  $B_s - B_f$  of specimens with various Ni contents.

### 3.5. Original austenite grain size

As demonstrated in Ref. [32], larger austenite grains finally lead to longer bainite sheaves. Generally, the smaller austenite grains result in more grain boundaries, which impose more restrictions on the growth of bainite sheaves. On account of controlling the amount of nucleation sites and growth rate, the morphological characteristics of bainite were significantly influenced by the austenite grain size. For nucleation, the grain boundary area decreases with increasing austenite grain size, causing fewer nucleation sites<sup>[33]</sup>. Furthermore, both nucleation is slower and the final bainitic ferrite length is larger in the specimens with coarser austenite grains than those in the specimens with finer austenite grains. During growth, both the width and the length of bainitic ferrite are larger in the specimens with coarser austenite grains than in the specimens with finer ones. Once impinging on the grain boundary, the growing bainite sheaves are restrained because the bainite sheaves could not traverse grain boundary. Fig. 9 shows the morphology of corresponding specimens during isothermal holding at 1350 °C for 240 s. In this study, grain size was calculated by the average value between the macroaxis and brachyaxis of itself, which was regarded to be spherical or spheroidal. In addition, Fig. 10 shows the variation of average grain size obtained by more than 40 measurements per specimen, whilst during the weld process, the grain grew irregularly for being unevenly heated, and thus the average grain size cannot represent the variation entirely. Analysis on positively skewed distribution of data has been utilized to avoid the mentioned deficiency, as shown in Fig. 11.



(a) W1, 5 °C/s; (b) W2, 5 °C/s; (c) W3, 5 °C/s; (d) W4, 5 °C/s;  
(e) W1, 1 °C/s; (f) W2, 1 °C/s; (g) W3, 1 °C/s; (h) W4, 1 °C/s.

**Fig. 9.** In-situ observation of morphology during isothermal holding at 1350 °C for 240 s when cooling at different rates.

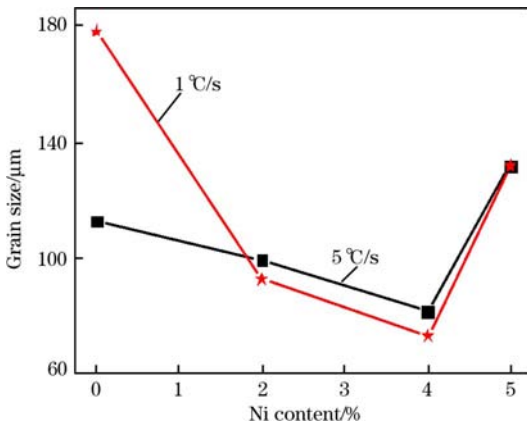


**Fig. 10.** Variation of average grain size with various Ni contents.

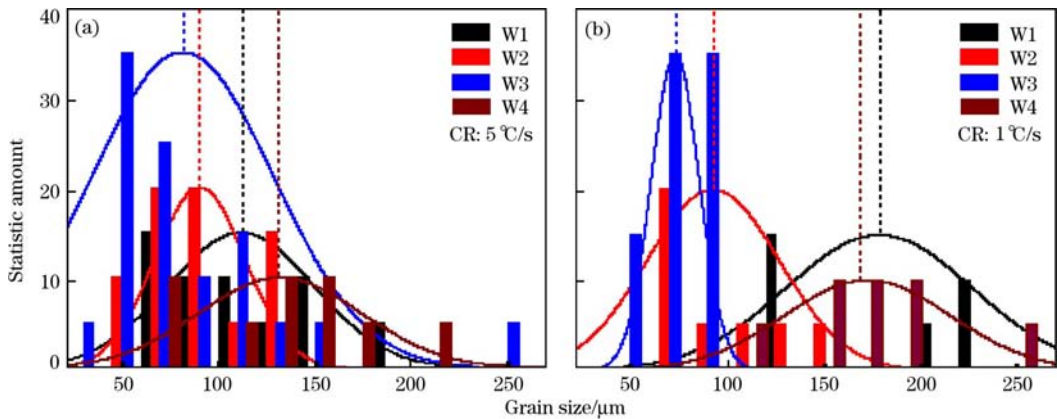


**Fig. 11.** Statistics of variation trend of average grain size.

**Table 6**

Ni equivalent for different specimens

Specimen	W1	W2	W3	W4
$Ni_{eq}/\%$	2.2	4.6	5.9	7

be solidified directly to austenite without peritectic reaction or  $\delta \rightarrow \gamma$  transformation, making final columnar  $\gamma$  crystals grow extensively. As previously described, small columnar crystals were closely relevant with  $Ni_{eq}$  between 3.4% and 6.2% because this  $Ni_{eq}$  could cause a peritectic reaction as the weld melt solidified. However, large columnar crystals would be generated by a higher  $Ni_{eq}$  owing to direct solidification into austenite and subsequently continuous growth of the liquid weld. When  $Ni_{eq}$  is lower than 3.4%, a simple  $L \rightarrow \delta$ -ferrite process of solidification would occur and instant columnar crystals would form. The ultimate microstructure and the mechanical properties of the WMs will be consequently influenced by the varying columnar crystal sizes.

## 4. Conclusions

(1) The final surface morphologies of various speci-

mens are: flat state merely without Ni, a minority of inconspicuous surface relief ( $w(Ni) \leq 2\%$ ), and distinct bainite relief ( $w(Ni) \geq 4\%$ ), which is in accordance with their microstructure—ferrite and granular bainite ( $w(Ni) \leq 2\%$ ), and lath bainite ( $w(Ni) \geq 4\%$ ). (2) With lower content of Ni ( $w(Ni) \leq 2\%$ ), the type of microstructure hardly depends on the Ni content but the cooling rate that was employed for the specimens; on the contrary, when Ni content arrives at a higher level ( $w(Ni) \geq 4\%$ ), lath bainite dominates the majority of microstructure at any cooling rate. (3) With the increment of Ni content, the value of  $B_s$ ,  $B_f$  and  $B_s - B_f$  decreases respectively. The three values obtained through cooling at 5 °C/s are lower than those at 1 °C/s for the higher cooling velocity increases the supercooling degree and provides enough driving force for phase transformation. The original austenite grain size is initially depressed and subsequently coarsened dramatically with the addition of Ni content. (4) In real welding process, Ni added into metal powder cored wires should be controlled nearly at the level of 4 wt.% to obtain finer prior austenite grain. Based on the level of Ni, the cooling rate of 5 °C/s is

preferred to refine grain and obtain more bainite for reheated zones to improve mechanical properties of WM.

## Acknowledgement

This work was financially supported by National Natural Science Foundation of China (No. 51675255), Pre-research of National Basic Research Program of China (2014CB660810), and the Rose Willow Outstanding Individual Programs of Lanzhou University of Technology (J201203).

## References

- [1] A. Barbacki, *J. Mater. Process. Technol.* 53 (1995) 57–63.
- [2] H. K. D. H. Bhadeshia, J. W. Christian, *Metall. Trans. A* 21 (1990) 767–797.
- [3] H. K. D. H. Bhadeshia, *Mater. Sci. Technol.* 15 (1999) 22–29.
- [4] A. Lambert-Perlade, A. F. Gourgues, A. Pineau, *Acta Mater.* 52 (2004) 2337–2348.
- [5] S. G. Park, K. H. Lee, K. D. Min, M. C. Kim, B. S. Lee, *Met. Mater. Int.* 19 (2013) 4954–4959.
- [6] Z. Y. Zhang, R. A. Farrar, *J. Mater. Sci.* 30 (1995) 5581–5588.
- [7] F. G. Caballero, H. K. D. H. Bhadeshia, K. J. A. Mawella, D. G. Jones, P. Brown, *Mater. Sci. Technol.* 17 (2001) 512–516.
- [8] F. G. Caballero, M. K. Miller, C. Garcia-Mateo, C. Capdevila, C. Garcia de Andres, *JOM* 60 (2008) 16–21.
- [9] H. Y. Li, X. W. Lu, X. C. Wu, *Mater. Sci. Eng. A* 527 (2010) 6255–6260.
- [10] H. G. Lambers, D. Canadinc, H. J. Maier, *Mater. Sci. Eng. A* 541 (2012) 73–80.
- [11] S. Das, I. Timokhina, S. B. Singh, *Mater. Sci. Eng. A* 534 (2012) 485–494.
- [12] K. Y. Zhu, C. Oberbillig, C. Musik, *Mater. Sci. Eng. A* 528 (2011) 4222–4231.
- [13] Y. Komiozo, Investigation for Microstructure and Toughness of Low Carbon and Low Alloy Steel Weld Metal, Osaka University, Osaka, 1982, pp. 100–112.
- [14] H. Terasaki, Y. Komizo, M. Yonemura, T. Osuki, *Metall. Mater. Trans. A* 37 (2006) 1261–1266.
- [15] M. K. Kang, M. X. Zhang, M. Zhu, *Acta Mater.* 54 (2006) 2121–2129.
- [16] D. Zhang, H. Terasaki, Y. I. Komizo, *J. Alloy. Compd.* 484 (2009) 929–933.
- [17] T. Hidenori, S. Yutaro, T. Atsushi, *Metall. Mater. Trans. A* 45 (2014) 3554–3559.
- [18] P. Kolmskog, A. Borgenstam, M. Hillert, *Metall. Mater. Trans. A* 43 (2012) 4984–4988.
- [19] M. A. Quintana, S. S. Babu, J. Major, C. Dallam, M. James, in: Proceedings of the 8th International Pipeline Conference, Volume 2, IPC2010, International Petroleum Technology Institute and the Pipeline Division, Alberta, Canada, 2010, pp. 599–608.
- [20] G. Xu, F. Liu, L. Wang, H. J. Hu, *Scripta Mater.* 68 (2013) 833–837.
- [21] H. Terasaki, Y. Komizo, *Sci. Technol. Weld Join.* 11 (2006) 561–566.
- [22] T. Ko, S. A. Cottrell, *J. Iron Steel Inst.* 172 (1952) 307–312.
- [23] A. J. Craven, K. He, L. A. J. Garvie, T. N. Baker, *Acta Mater.* 48 (2000) 3857–3868.
- [24] S. G. Hong, K. B. Kang, C. G. Park, *Scripta Mater.* 46 (2002) 163–168.
- [25] S. Zhao, D. L. Wei, R. B. Li, L. Zhang, *Mater. Trans.* 55 (2014) 1274–1279.
- [26] S. E. Offerman, N. H. van Dijk, J. Sietsma, S. Grigull, E. M. Lauridsen, L. Margulies, H. F. Poulsen, M. Th. Rekveldt, S. van der Zwaag, *Science* 298 (2002) 1003–1005.
- [27] J. W. Christian, *The Theory of Transformations in Metals and Alloys: Part I*, 3rd ed., Oxford, London, 1975.
- [28] H. K. D. H. Bhadeshia, A. R. Waugh, *Acta Metall.* 30 (1982) 775–784.
- [29] S. K. Ghosh, N. Bhowmik, A. Haldar, A. A. Chattopadhyay, *Mater. Sci. Eng. A* 527 (2010) 1082–1088.
- [30] L. Y. Lan, C. L. Qiu, D. W. Zhao, X. H. Gao, L. X. Du, *J. Mater. Sci.* 48 (2013) 4356–4364.
- [31] Y. Arai, T. Emi, H. Fredrilsson, H. Shibata, *Metall. Mater. Trans. A* 36 (2005) 3065–3074.
- [32] H. J. Hu, G. Xu, F. Liu, L. Wang, L. X. Zhou, Z. L. Xue, *Trans. Mater. Heat Treat.* 35 (2014) 83–87 (in Chinese).
- [33] T. Kvackaj, I. Mamuzic, *ISIJ Int.* 38 (1998) 1270–1276.
- [34] J. F. Lancaster, *Metallurgy of Welding*, 2nd ed., George & Unwin, London, 1980.